

# Unsteady aerodynamic model of a cargo container for slung-load simulation

**L. S. Cicolani and J. G. A. da Silva**

Army/NASA Rotorcraft Division, Ames Research Center  
Moffett Field  
California, USA

**E. P. N. Duque**

Department of Mechanical Engineering  
Northern Arizona University  
Flagstaff, Arizona, USA

**M. B. Tischler**

Army/NASA Rotorcraft Division, Aeroflightdynamics Directorate, (AMRDEC) US Army Research Development and Engineering Command,  
Moffett Field,  
California, USA

## ABSTRACT

The problem of simulation models capable of predicting the aerodynamic instability of helicopter slung-load cargo containers and bluff bodies is addressed. Instability for these loads is known to depend on unsteady frequency-dependent aerodynamics, but simulation models that include the unsteady aerodynamics do not currently exist. This paper presents a method for generating such models using computational fluid dynamics (CFD) to generate forced-oscillation aerodynamic data and frequency domain system identification techniques to generate a frequency response from the CFD data and to identify a transfer function fit to the frequency response. The method is independent of the responsible flow phenomenon and is expected to apply to bluff-bodies generally. Preliminary results are presented for the case of the 6- by 6- by 8-ft CONEX (container express) cargo container. The present work is based on two-dimensional (2D) aerodynamic data for the CONEX side force and yaw moment generated by a forced oscillation in which frequency is varied smoothly over the range of interest. A first-order rational polynomial transfer function is found adequate to fit the aerodynamics, and this is shown to provide a good match with flight test data for the yawing motion of the CONEX.

## NOMENCLATURE

$a_\infty$	free-stream speed of sound (ft/sec)
$CD$	drag coefficient
$CS$	side force coefficient
$CN$	yaw moment coefficient
$I_{ZZ}$	inertia about the body vertical axis (ft-lb-sec <sup>2</sup> )
$K_r$	swivel friction coefficient (ft-lb-sec)
$L$	reference length (ft)
$M$	Mach number
$q$	dynamic pressure (lb/ft <sup>2</sup> ) or pitch rate (rad/sec)
$r$	yaw rate (rad/sec)
$Re$	Reynolds number
$s$	Laplace transform variable (rad/sec)
$ST$	Strouhal number
$V$	airspeed (knots)
$\alpha$	angle of attack (deg)
$\beta$	sideslip angle (deg)
$\tau$	time delay or time constant (sec)
$\omega$	frequency (rad/sec)



Figure 1. UH60 – CONEX slung load configuration.

## 1.0 INTRODUCTION

Carrying underslung loads has long been one of the many applications of helicopters, in both military and civil operations. The load, however, introduces extra dynamics to the system, including potential load aerodynamic instabilities, which can reduce the speed envelope well below the power-limited speed of the aircraft-load configuration. Load-helicopter combinations are certified mostly by means of flight tests. Accounting for the diversity of possible loads<sup>(1)</sup> and the exploratory nature of the certification makes this procedure expensive, time-consuming, and sometimes dangerous. Therefore, simulations are a potentially efficient tool in the pre-evaluation of the flight envelope and the development of stabilisation devices. To date, however, simulations have been inadequate in the case of cargo containers and other bluff bodies because the load aerodynamics have been based on static aerodynamics, whereas stability for these loads has previously been shown to be due to unsteady aerodynamic effects<sup>(2,3,4)</sup>.

The modelling of unsteady aerodynamics associated with slung loads has been the subject of several studies, most of them carried out in the 1970s and focused on the 8ft by 8ft by 20ft MILVAN cargo container. In Refs 2 and 3 it was shown that the use of quasi-steady derivatives alone was unsuccessful in predicting slung-load instabilities, and that subjecting bluff bodies to forced oscillations yielded frequency-dependent aerodynamic coefficients. In Refs 2-4 the cause of unsteady aerodynamic effects was identified with the existence of appreciable phase lags in the growth and decay of separation bubbles and with vortex shedding. From these studies, it can be concluded that bluff body aerodynamics comprise the following components: static aerodynamics, viscous damping due to angular rates, unsteady aerodynamics of the stationary container due to vortex shedding, and unsteady aerodynamics of an oscillating container due to phase lags in separation bubble growth and vortex shedding.

Two approaches have been taken previously in modelling unsteady load aerodynamics. The first approach, in work done at Northrop<sup>(4)</sup> and at the University of Bristol<sup>(2,3)</sup> and in Ref. 5 is to account for the observed oscillatory motions by introducing hysteresis in the moment function. This was based either on modelling the

responsible flow phenomena (suction pressure distribution in the separation bubbles and lagged effects of angle rates), or on hypothesising a model structure for the aerodynamic coefficients that reproduces the observed limit cycle oscillations and tuning the model parameters to the measured motions. The second approach, proposed in Ref. 6, is to identify the aerodynamic coefficients from forced-oscillation input-output aerodynamic data. This approach makes no assumptions about the responsible flow phenomenon and can be applied to any load.

This paper adopts the approach from Ref. 6. The current effort benefits from the advent of computational fluid dynamics (CFD) codes that, after validation for the specific application, can rapidly provide considerable unsteady flow aerodynamic data compared to wind tunnel and flight test sources. The effort also benefits from frequency domain identification software that can generate frequency responses from time-history data over the frequency range of interest and fit these responses with a model of the aerodynamics. The paper applies this approach to the 6ft by 6ft by 8-ft CONEX cargo container (Fig. 1), which has been the subject of previous slung-load studies, including flight testing<sup>(7)</sup>, wind tunnel measurement of its static aerodynamics<sup>(8)</sup>, and simulation studies<sup>(9)</sup>. The goal of this work is to develop a modelling method, or model structure, that captures the unsteady aerodynamics of bluff bodies and can predict slung-load instabilities. This paper reports initial results in that effort.

This paper first discusses the CFD method, the flow characteristics of the CONEX, and the forced oscillation inputs and corresponding aerodynamic outputs. Then the frequency responses are presented along with a discussion of the effects of amplitude, frequency, reference sideslip angle, and velocity. A transfer function model is defined and fitted to

the responses and, finally, simulation results are given. The present study uses two-dimensional (2D) aerodynamics and focuses on the directional motions of the CONEX. The 2D aerodynamics suffice for estimates of side force and yaw moment, which are close to the 3D values, and also avoids the excessive computation time requirements for 3D unsteady flow computations. The lateral-directional degrees of freedom are thought to account for the instabilities of cargo containers.

## 2.0 APPLICATION OF CFD TO THE CONEX

The prediction of unsteady aerodynamic forces on bluff bodies such as the CONEX requires time-accurate solution of the Navier-Stokes equations. A solution method must be able to accurately capture the viscous boundary layer flows as well as the unsteady and complex flow structures associated with vortex shedding. In addition, the method must have the ability to simulate dynamic body motions, either specified forced oscillations or general motions due to aerodynamic forces.

The code chosen for this study is a Reynolds-averaged Navier-Stokes solver known as OVERFLOW-D. The OVERFLOW algorithm was first developed by Buning *et al* for fixed wing applications<sup>(10,11)</sup> and further developed by the U. S. Army for rotorcraft applications<sup>(12-14)</sup>. This code is suited to unsteady compressible flows and arbitrary body motions, as demonstrated in previous applications to unsteady rotorcraft blade motion and aircraft store separation simulations, and it can compute both 2D and 3D aerodynamics. Other algorithms that might be considered for such unsteady separated flows include the Detached Eddy Simulation, the Large Eddy Simulation<sup>(15)</sup>, and the commercial code STAR-CD<sup>TM(16)</sup>, but computation time requirements might be prohibitive for these codes.

Code options and parameter values related to integration schemes and dimensionless time step, grid details and extent, boundary conditions, and turbulence model were selected for accuracy in the CONEX application. Details of these aspects of the computational scheme are given in the appendix and in Ref. 17.

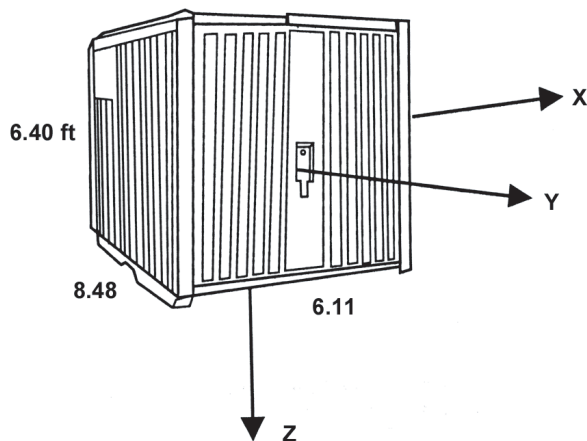


Figure 2. CONEX.

2.1 Computations

The CONEX is illustrated in Fig. 2, along with its dimensions and the body axes orientation for this study. CFD computations were made for a rectangular box with the full-scale CONEX dimensions but omitting such CONEX details as skids and surface corrugations. The range of airspeeds of interest for the CONEX aerodynamic model is about 130kt and below.

The CFD computations were performed for Reynolds number  $3.91 \times 10^6$  (which corresponds to the full-scale CONEX at 60kt with reference length 6.11ft), and Mach number 0.2 (132kt). The Mach number for the CFD work is an approximate minimum required to maintain solution accuracy for the current version of the compressible OVERFLOW-D code. The aerodynamic coefficients are nearly invariant with Mach number over the speed range of interest

for the CONEX, and the variations with time can be scaled to other Mach numbers by scaling the dimensionless time of the CFD data to the desired Mach number,  $M$ , using:

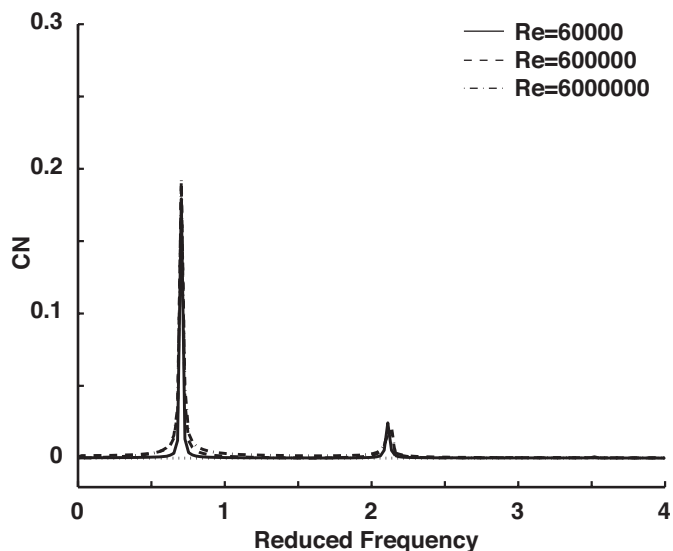
$$t(M) = k \Delta \bar{t} \frac{M_{CFD}}{M} \frac{L}{a_\infty} \dots (1)$$

where  $i$  is real time,  $k$  is the time-step index,  $\Delta \bar{t}$  is the dimensionless time step used in the computations, ( $\Delta \bar{t} \equiv \Delta t a_\infty / L$ ),  $a_\infty$  is the free-stream speed of sound, and  $L$  is the reference length. In addition, the

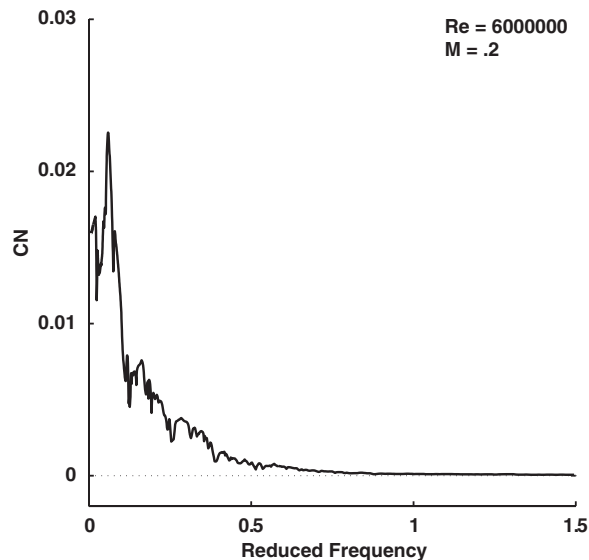
aerodynamics of bluff bodies are generally expected to be nearly invariant with Reynolds number over the range of Reynolds numbers from wind tunnel models to full scale. This is demonstrated for the CONEX in Fig. 3(a). The figure shows the frequency spectrum of the yaw moment coefficient for the 2D aerodynamics with the body at a fixed attitude ( $\beta = 0$ ) vs reduced frequency or Strouhal number,  $S_T = \omega L / V$ , for three Reynolds numbers separated by two orders of magnitude and covering the range from wind tunnel models to full scale. Peaks occur at the frequency of the background vortex shedding of the unsteady flow and its harmonics. As seen, the Strouhal number for the peak is invariant with Reynolds number, and is identified as 0.70 (based on frequency in rad/sec). A similar plot for Mach numbers (not shown) demonstrated a similar invariance with Mach number over the range of interest for the CONEX.

The computational setup was validated by a comprehensive comparison of 3D static aerodynamic results from quasi-static computations with wind tunnel data<sup>(8)</sup>. Yaw moment, drag, and side force are compared in Fig. 4. Yaw moment shows excellent agreement in magnitude and variation with sideslip angle at all angles of attack, whereas drag is somewhat underestimated by the CFD at low sideslip angles, but shows good gross agreement in magnitude. Differences are due in part to the absence of skids in the CFD model as well as residual errors in both the CFD and wind tunnel results. A more detailed comparison is given in Ref. 18. In addition, the 2D unsteady flow computations were validated against experiment in the case of a square cross section (see appendix). For the CONEX 2D cross section (aspect ratio 1.4) there is no experimental literature. However, the Strouhal number given here, (0.11 based on frequency in Hz) is bracketed by numbers given from wind tunnel studies in Ref. 19 at aspect ratios of 1 ( $S_T = 0.13$ ) and 2 ( $S_T = 0.085$ ) for Reynolds numbers above 10,000.

All CFD computations were performed on the 32-processor Renewable Energy CFD Laboratory Compute cluster at Northern Arizona University. The CFD computations for this work included the 2D and 3D static aerodynamics and 2D aerodynamic time history data for forced oscillations at both fixed frequencies and frequencies varying smoothly over the range of interest (frequency sweep). The frequency sweep required 500,000 time steps. The 2D computations used 83,000 grid points and required 50 CPU hours using two 1.8GHz processors. The estimated time for 3D computations of the frequency sweep (1.5 million grid points, eight processors) is two to four weeks, depending on the time accuracy required. The development work of this paper is based on the 2D aerodynamics because of the difference in computation time and because the present preliminary study is limited to modelling the directional aerodynamics.



(a) 2D aerodynamics.



(b) 3D aerodynamics

Figure 3. Yaw moment frequency spectrum.

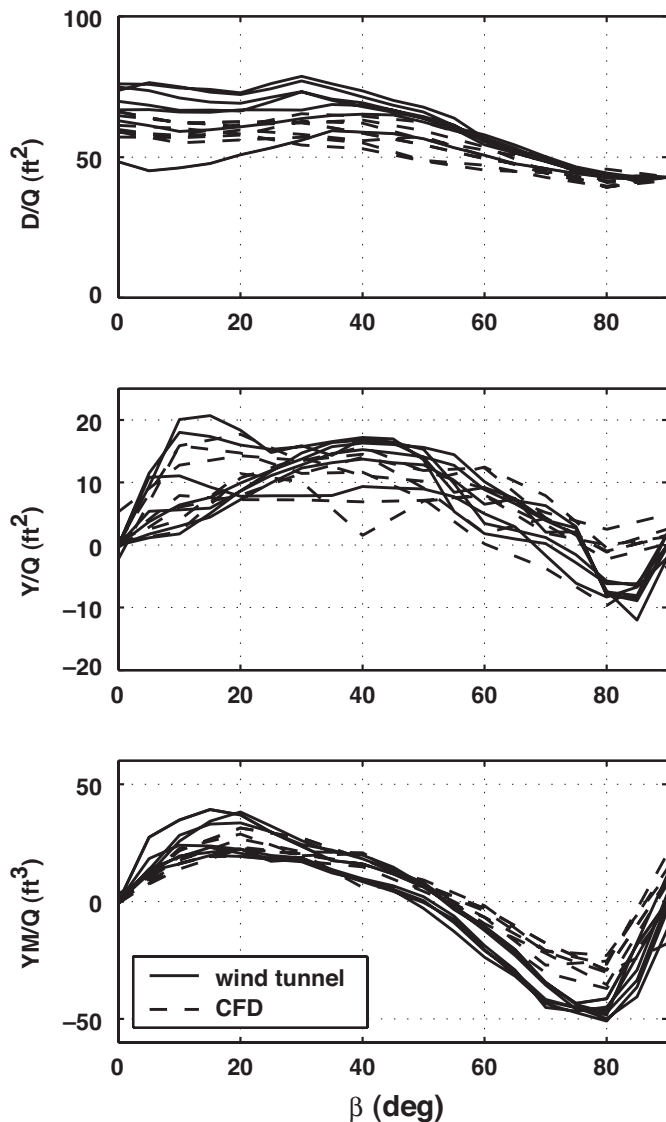


Figure 4. Comparison of 3D CFD and wind-tunnel CONEX static aerodynamics:  $\alpha = [-90:30:90]$ .

2.2 Flow structure

Velocity contours of the 3D flow around the horizontal centre plane of the CONEX are shown in Fig. 5. This illustrates the large separation bubbles of low velocity recirculating flow that exist over the sides of the CONEX at zero sideslip and the massive wake extending downstream from the CONEX. At other orientations to the flow, the bubbles enlarge on the downstream side and reduce or disappear on the upstream side. Similar flow structures were documented for the MILVAN in the wind tunnel work in Refs 2 and 3.

In addition, the wake is unsteady; that is, vortices are periodically shed into the wake alternately from the top and bottom rear corners, even when attitude is fixed. A snapshot of pressure contours in the extended wake of the 2D flow is shown in Fig. 6. A vortex 'street' of successive pressure minima marking the centres of vortices is clearly visible. The background vortex shedding occurs at a Strouhal number that is invariant with airspeed and was estimated at 0.70 for the CONEX 2D flow (Fig. 3(a)). The corresponding physical frequency varies with velocity, as specified by its Strouhal number, and increases linearly with airspeed. The background vortex shedding results in continual oscillations of the aerodynamic coefficients at the vortex shedding frequency.

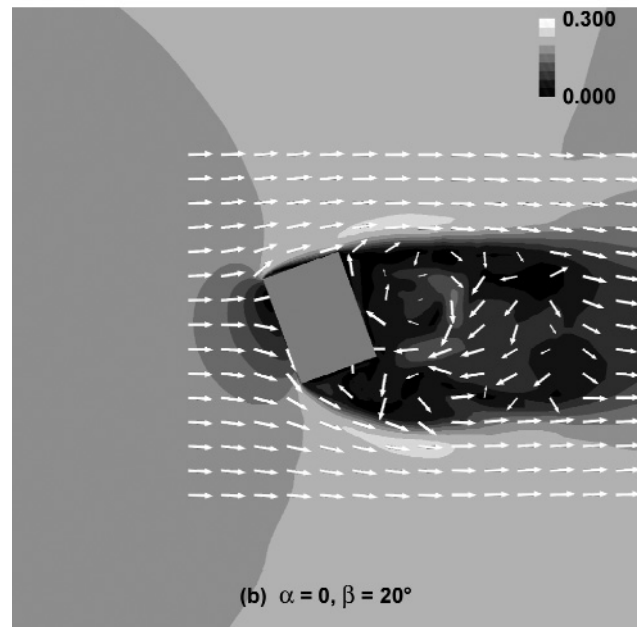
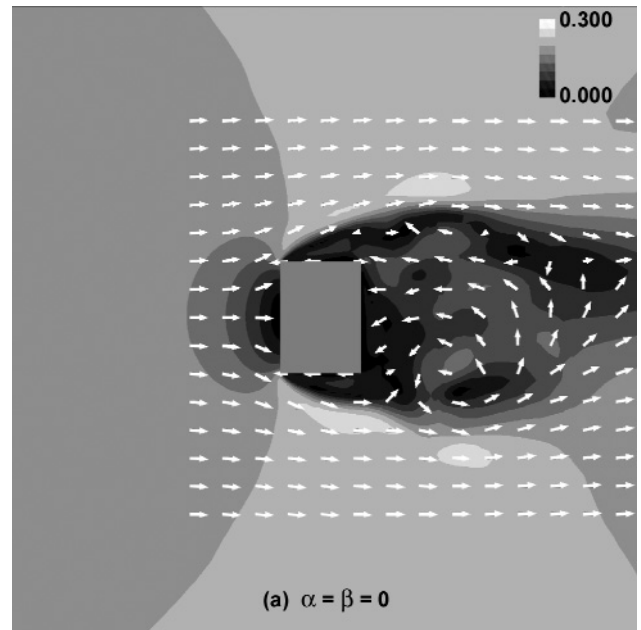


Figure 5. CONEX mach number contours (3D aerodynamics).

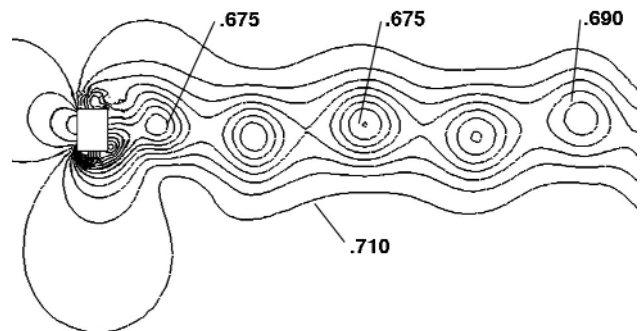


Figure 6. CONEX pressure contours ( $P/\rho a^2$ ), 2D flow, freestream pressure = 0.714.

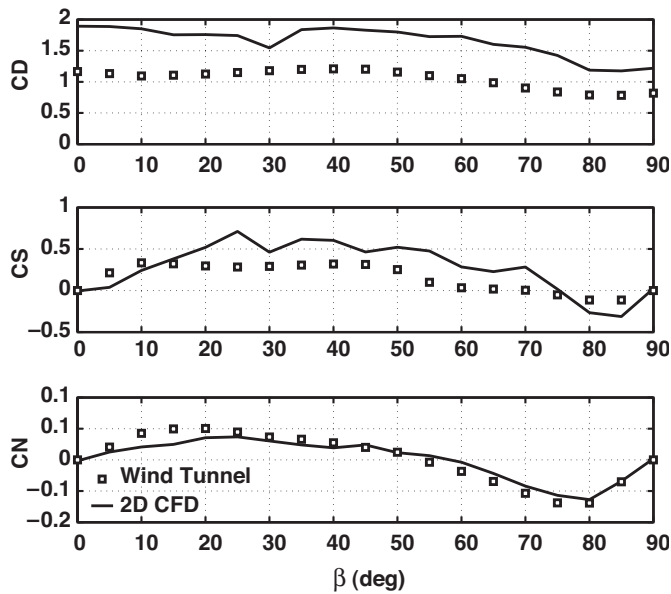


Figure 7. Comparison of 2D CFD and 3D wind tunnel data ( $\alpha = 0$ ).

During oscillations of the body, the mean flow structure lags the mean steady state structure corresponding to the instantaneous attitude, and there are corresponding lags in the mean aerodynamic forces and moments. For large enough oscillation amplitude, vortices are left behind at the rear corner of the downstream side as the CONEX retreats from the sideslip angle extreme, and this occurs at the frequency of the oscillation. Animations of the 2D flow for both the stationary and oscillating CONEX can be seen in Ref. 20.

### 2.3 2D vs 3D aerodynamics

The frequency-response analysis in the present initial phase of the modelling effort will use 2D aerodynamics for the  $x$ - $y$  cross section of the CONEX. A comparison of 2D CFD data and 3D wind tunnel data for the static aerodynamics at  $\alpha = 0$  is shown in Fig. 7. There is good agreement in magnitude, zeros, and trends for yaw moment and moderate agreement for side force, while drag differs by a factor of about 1.7. A similar difference between 2D and 3D drag is known in the literature on flat plate and cube aerodynamics, but this difference does not affect the present work, which considers only the unsteady side force and yaw moment. The frequency spectrum of the yaw moment coefficient for the 3D aerodynamics is shown in Fig. 3(b). The isolated peaks seen in the 2D spectrum have disappeared, power is confined to lower frequencies, and the amplitude scale is an order of magnitude smaller. This indicates that the unsteady effects of the 2D flow are significantly attenuated in the 3D flow. Although these comparisons suggest the low-frequency behaviour of the coefficients of interest will be captured by the 2D aerodynamics, the implications for the responses to forced oscillations at higher frequencies cannot yet be evaluated. The present study is, therefore, a preliminary evaluation of the proposed modelling approach prior to generating forced-oscillation data for the 3D flow.

## 3.0 MODELLING APPROACH

### 3.1 Concept

In flight-dynamics simulations, the aerodynamics model provides a relation between the flow variables (incidence angle of interacting body, velocity, air properties, etc.) and the aerodynamic forces and moments produced. To include the dynamic effects of unsteady flow, the

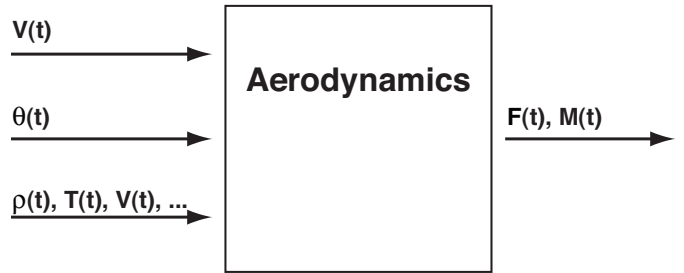


Figure 8. General aerodynamic system.

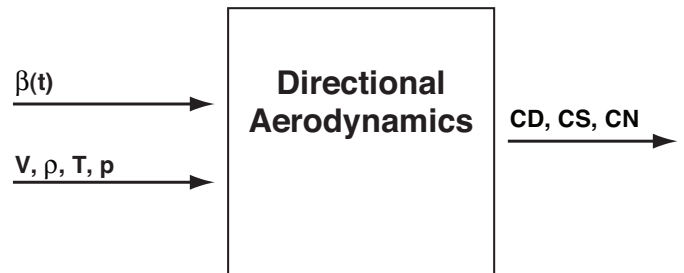


Figure 9. Directional aerodynamic system.

aerodynamics of a body can be viewed like any other dynamical system, with outputs such as forces and moments, and with inputs such as incidence angles, flow velocity, density, temperature, etc. (Fig. 8). In applications, the timescale separation between the flow dynamics and the driving inputs is usually large enough to consider the outputs as time invariant, thereby reducing the aerodynamics to a static problem. In some cases quasi-static terms dependent on input derivatives  $\dot{\alpha}, \dot{\beta}, \dot{p}, \dot{q}, \dot{r}$  are reincluded. These are computed from behaviour in the vicinity of zero rates. However, wind-tunnel studies of bluff bodies have shown that static and quasi-static descriptions are insufficient to fully characterise their aerodynamics. This results from the nature of the flow around such bodies, which is dominated by massive separations involving large timescales. Thus, given the increase of the flow timescale toward that of the driving inputs, the aerodynamic forces and moments can no longer be considered time invariant. As wind-tunnel studies indicate in the case of cargo containers, this is mainly reflected in the interaction between the incidence angle and the separation bubble growth, resulting in the latter lagging the motion. In this case, only the incidence angle varies in a timescale similar to that of the flow dynamics, whereas all the other inputs, such as velocity and air properties, vary slowly enough to be considered time invariant. The outcome is then a dynamic system affected by the time-varying input vector  $\theta(t)$ , defining the incidence of the load, as well as by time-invariant inputs defining the magnitude of the flow velocity  $V$  and the free-stream air properties.

For this initial study of the problem, we further simplify from the 3D aerodynamic system (three input angles, six output force and moment components) to a 2D system that drives the slung-load lateral-directional dynamics (Fig. 9). This neglects some, but not all, of the aerodynamic couplings. Furthermore, given that the CONEX has a nearly cubic shape, then no significant changes are expected between the flow phenomena governing the aerodynamics of the lateral-directional and the longitudinal dynamics. The 2D system has a single input (sideslip) and three outputs (drag, side force, yaw moment), which require three independent input-output relations. Each of these relations can be represented in the frequency domain by a rational transfer function:

$$\begin{aligned} \frac{CD(s)}{\Delta\beta(s)} &= T_{D,\beta} \\ \frac{CS(s)}{\Delta\beta(s)} &= T_{S,\beta} \\ \frac{CN(s)}{\Delta\beta(s)} &= T_{N,\beta} \end{aligned} \quad \dots (2)$$

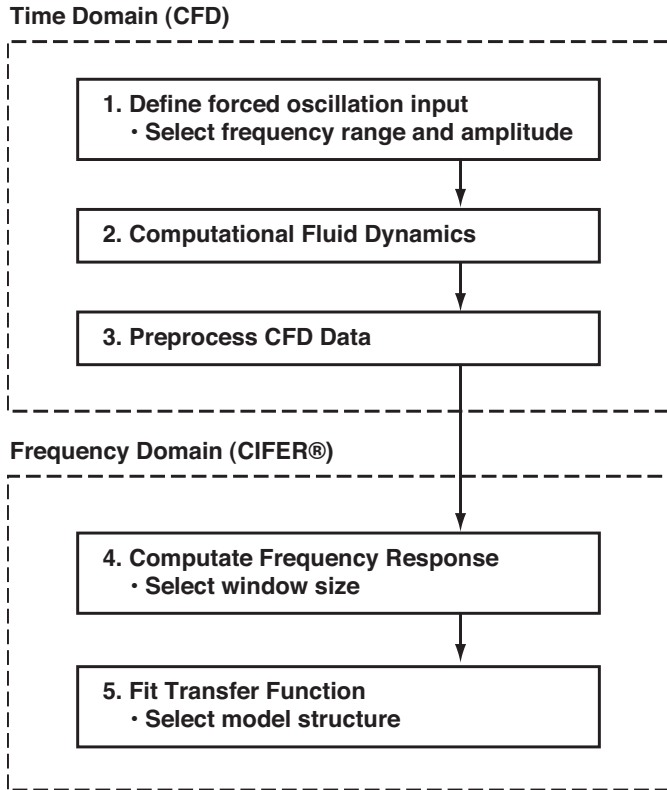


Figure 10. Development procedure for unsteady aerodynamics model.

In Ref. 6 a model for the 8- × 8- × 20ft MILVAN cargo container was derived using limited wind-tunnel data from Ref. 3. It was found that a rational transfer function with second-order numerator and denominator was adequate to represent the container aerodynamics throughout the frequency range of the data. The second-order transfer function has the form:

$$\frac{CN(s)}{\Delta\beta(s)} = \frac{a_2s^2 + a_1s + a_0}{b_2s^2 + b_1s + 1} \dots (3)$$

This can be transformed to the time domain and rearranged to the following differential equation:

$$CN(t) = a_0 \Delta\beta(t) + a_1 \dot{\Delta\beta}(t) + a_2 \ddot{\Delta\beta}(t) - b_1 \dot{CN}(t) - b_2 \ddot{CN}(t) \dots (4)$$

Collecting terms:

$$CN(t) = a_0 \Delta\beta(t) + a_1 \dot{\Delta\beta}(t) + CN_{unsteady} \dots (5)$$

where  $CN_{unsteady}$  denotes the yaw moment contribution due to unsteady aerodynamic effects from higher-order angle derivatives and other terms:

$$CN_{unsteady} = a_2 \ddot{\Delta\beta}(t) - b_1 \dot{CN}(t) - b_2 \ddot{CN}(t) \dots (6)$$

Similar transfer functions apply to the other coefficients. For first- and second-order functions, the static and quasi-static derivatives can be identified with the coefficients of the polynomials by taking the appropriate limits:

$$CN_\beta = \lim_{\omega \rightarrow 0} (\text{Real}[T_{N,\beta}(j\omega)]) = a_0 \dots (7(a))$$

$$CN_r = \lim_{\omega \rightarrow 0} \left( \text{Imag} \left[ \frac{1}{\omega} T_{N,\beta}(j\omega) \right] \right) = a_1 - b_1 a_0 \dots (7(b))$$

Generally, the order of the transfer function is selected to minimise complexity while retaining adequate accuracy of fitting the available data. Derivatives with respect to yaw rate,  $r$ , are neglected in the model because there are no first-order sources of these effects, such as a vertical tail, so that flow lag effects represented by the sideslip derivative can be assumed to dominate the quasi-static angular rate effects.

### 3.2 Procedure

An approach based on system identification in the frequency domain was taken in the present effort to model the dynamics associated with bluff body aerodynamics. The three principal steps in the procedure are (1) obtain the response of the system to excitation over the frequency range of interest, (2) extract a frequency response (Fourier transform) from the input and output time histories, and (3) fit a transfer function to the frequency response. This approach is commonly used in control system analysis. It can be applied to any dynamic system, and in the case of bluff body aerodynamics, it makes no assumptions about the responsible flow phenomena and can be applied to any type of load.

The identification procedure for the present work is depicted in Fig. 10 and can be divided into five steps. First the input forced oscillation in sideslip angle is defined to excite the system over the desired frequency range and at an appropriate amplitude. This can be done using a set of fixed frequencies distributed over the desired frequency range, as has been done in wind tunnel studies, or using a single input time history in which the frequency varies continuously over the desired range (frequency sweep), as has been done in control system identification work. Second, this signal is used in the CFD simulation to generate the corresponding forced-oscillation aerodynamic data. Third, the CFD output and the input signals are preprocessed to remove data anomalies (dropouts and wild points), to scale the data from the dimensionless time of the CFD computations to real time at the reference speed of the present study (60kt), and to account for the inevitable differences between CFD and simulation conventions regarding axes, signs, reference areas, point about which moments are taken, etc.

Fourth, the frequency responses are computed using Fourier transform methods. The CIFER<sup>®(21)</sup> software package for frequency domain analysis in aeronautical applications was used. The frequency response represents the first harmonic approximation of the input-output dynamics. The residual signal associated with the higher-order harmonics is seen as noise in this approximation. The quality of the approximation is measured by the coherence function, which is the linear correlation between input and output as a function of frequency and has values in the interval (0,1]. Values above 0 × 6 are considered necessary for credible frequency-response results. Turbulence and uncorrelated or nonlinear dynamics all reduce the coherence function. A factor in the computations is the window size into which the Fourier analysis subdivides the time history. Results are better in particular frequency ranges according to the window size, and responses for different windows can be computed and optimally combined by CIFER to get the final frequency response.

The final step consists of fitting a transfer function to the frequency response over the frequency range with adequate coherence. The initial transfer function model structure is selected based on response complexity, physical insight, and accuracy of fit. The model structure is further refined by eliminating nearly cancelling pole-zero combinations, eliminating parameters for which the accuracy of the fit is insensitive, and treating parameters that are highly

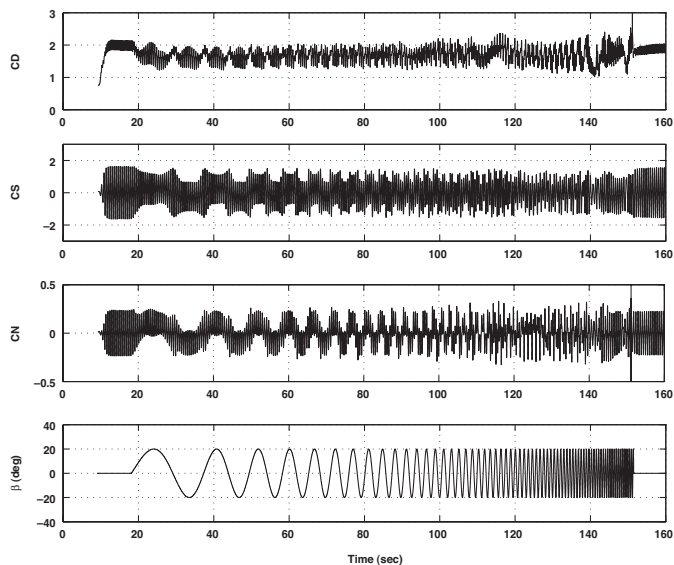


Figure 11. Aerodynamic response to frequency sweep:  $\beta_0 = 0$ , amplitude =  $20^\circ$ ,  $V = 60\text{kt}$ .

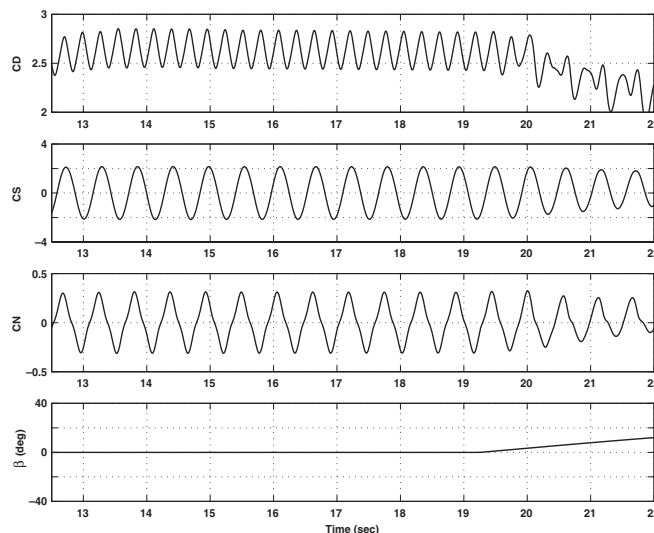


Figure 12. Oscillations due to vortex shedding.

### 4.0 TIME-HISTORY DATA

#### 4.1 Frequency sweep

In a frequency sweep input, frequency  $\omega$  is varied over the range of interest using the equations<sup>(22)</sup>.

$$\omega = \omega_{\min} + C_2 \left( e^{C_1 \frac{t}{t_{\text{sweep}}}} - 1 \right) (\omega_{\max} - \omega_{\min}) \quad \dots (8(a))$$

$$\theta = \int \omega dt \quad \dots (8(b))$$

$$\beta = \beta_0 + A \sin \theta \quad \dots (8(c))$$

Frequency varies exponentially from  $\omega_{\min}$  to  $\omega_{\max}$  during the time interval  $t_{\text{sweep}}$ . The parameters  $C_1$ , and  $C_2$  are empirically determined such that the coefficient factor in the equation varies from 0 to 1 over the sweep interval in a satisfactory way ( $C_1 = 4$ ,  $C_2 = 0.019$ ). An acceptable value for the sweep interval is three to five times the period of the minimum frequency. The forced oscillation angle  $\beta$  has amplitude  $A$  and varies about the mean angle  $\beta_0$ . The above equations were modified for the CFD computations in dimensionless time by replacing time and frequency with dimensionless time and reduced frequency.

The sweep gives uniform spectral content over the frequency range. This results in a smoother frequency response than can be obtained from a set of discrete frequencies distributed over the frequency range. In addition, the sweep requires only a single run that is only as long as would be required for a fixed-frequency run at the lowest frequency for a sufficient number of cycles.

#### 4.2 Sweep amplitude

The choice of amplitude is a compromise between large enough amplitude to allow proper growth of the separation bubbles and excitation of the unsteady aerodynamics, and small enough amplitude to avoid regions of excessive nonlinearity of the aerodynamics. The static aerodynamics vs sideslip are shown in Fig. 4 for reference. For example, the yaw moment coefficient reaches an extreme at  $20^\circ$  and then reverses itself to a

minimum near  $80^\circ$ . Amplitudes of  $10^\circ$ ,  $20^\circ$ , and  $45^\circ$  were considered. Frequency responses indicated that  $20^\circ$  amplitude provided reasonable linearity and good excitation of the unsteady aerodynamics, while  $10^\circ$  gave inadequate excitation and  $45^\circ$  encompassed excessive nonlinearity.

#### 4.3 Frequency range and sample time history

The frequency range of the computations should include the vortex shedding frequency in order to capture the effect of the interference between body oscillations and the flow dynamics. Fig. 11 shows the aerodynamic response (drag, side force, yaw moment coefficients) to a frequency sweep input around  $\beta_0 = 0$ . The response exhibits two frequencies: (1) the frequency of the driving oscillation, and (2) a higher constant frequency associated with vortex shedding that is present independent of the input frequency. The oscillations due to vortex shedding are visible in greater detail in Fig. 12, which shows the initial 10sec interval from Fig. 11 during which attitude is fixed. These oscillations are approximately sinusoidal, similar to an undamped natural mode in a dynamic system. The drag coefficient oscillates at twice the vortex shedding and input frequencies owing to its symmetry about zero sideslip angle. (This would not be the case at other angles.) Amplitudes at the vortex shedding frequency are somewhat larger than amplitudes due to the  $20^\circ$  forced oscillation. The side force and yaw moment oscillations due to vortex shedding are, surprisingly, larger than the extreme values of the 3D static aerodynamics for these coefficients, but are consistent with the fluctuations seen in wind tunnel and CFD studies of square and rectangular cylinders (e.g. Ref. 23). Here, the rms fluctuations are 0.10, 1.1, and 0.23 for  $CD$ ,  $CS$ , and  $CN$ , respectively. Additional details, including variations of these parameters with mean sideslip angle, are given in Ref. 18.

The data of Fig. 11, correspond to a flow velocity of 60kt at which the vortex shedding frequency is 11.3rad/sec. This frequency varies with velocity such that the corresponding Strouhal number is invariant. The range of Strouhal numbers used in the forced oscillation was (0.014, 0.82), which includes the vortex shedding Strouhal number, 0.70. The corresponding range of frequencies at 60kt is (0.25, 13.5)rad/sec.

In Fig. 11 and in the remaining results the reference airspeed is 60kt, input amplitude is  $20^\circ$ , 2D aerodynamics are used, the reference area and volume for the coefficients are the CONEX frontal area and volume, respectively, and moments are computed about the geometric centre of the CONEX.

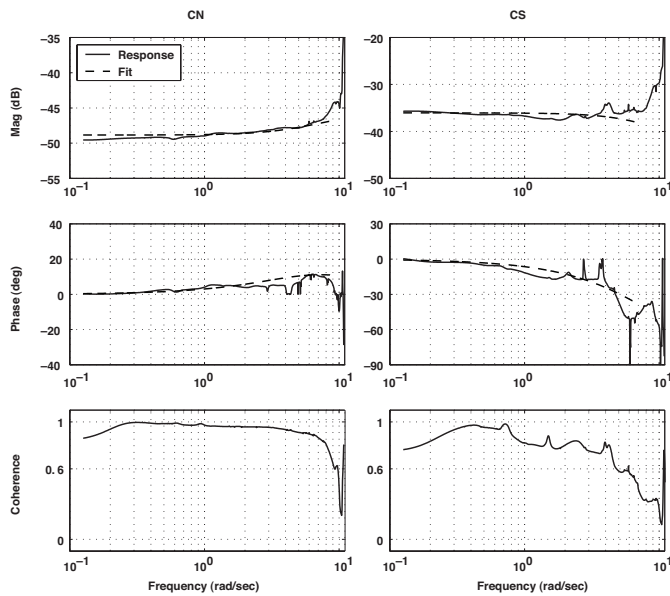


Figure 13. Frequency response and transfer function fit;  $\beta_0 = 0, 60\text{kt}$ .

## 5.0 FREQUENCY DOMAIN RESULTS

### 5.1 Transfer-function fits ( $\beta_0 = 0, 60\text{kt}$ )

The frequency response is a linear description of the response to oscillations around the reference sideslip angle. Frequency responses for *CN* and *CS* in the vicinity of  $\beta_0 = 0$  are shown in Fig. 13. Responses were computed for five window sizes and these were combined optimally by CIFER to get the final response. The smaller windows give better coherence at higher frequencies, and conversely, and the largest window defines the minimum frequency in the computed response. The largest window used should be no larger than one-third of the record length. In the result (Fig. 13), the *CN* response loses adequate coherence at 9rad/sec and above, while the *CS* response loses adequate coherence at 7rad/sec and above.

Transfer-function fits to the responses were made over the frequency range with adequate coherence. Coherence-weighted fits were generated with the CIFER fitting utility. For *CN* it was found that first-order numerator and denominator

### 5.2 Frequency response near the vortex shedding frequency

In the *CN* response around  $\beta_0 = 0$  (Fig. 13) coherence drops below acceptable values for forcing frequencies above 9rad/sec, so that behaviour across the vortex shedding frequency at 11.3rad/sec is poorly defined in these results. However, the available results capture the

Table 1  
Transfer-function model at  $\beta_0 = 0, V = 60\text{kt}$

$\frac{CN(s)}{\Delta\beta(s)} = \frac{a_1 s + CN_\beta}{\tau s + 1}$	$\frac{CS(s)}{\Delta\beta(s)} = \frac{a_1 s + CS_\beta}{\tau s + 1}$		
$\tau$ (sec)	0.113	$\tau$	0.113
$a_1$ (sec/deg)	0.000836	$a_1$	0
$CN_\beta$ (deg <sup>-1</sup> )	0.00501	$CS_\beta$	0.0219
Cost	7.7	Cost	30.1

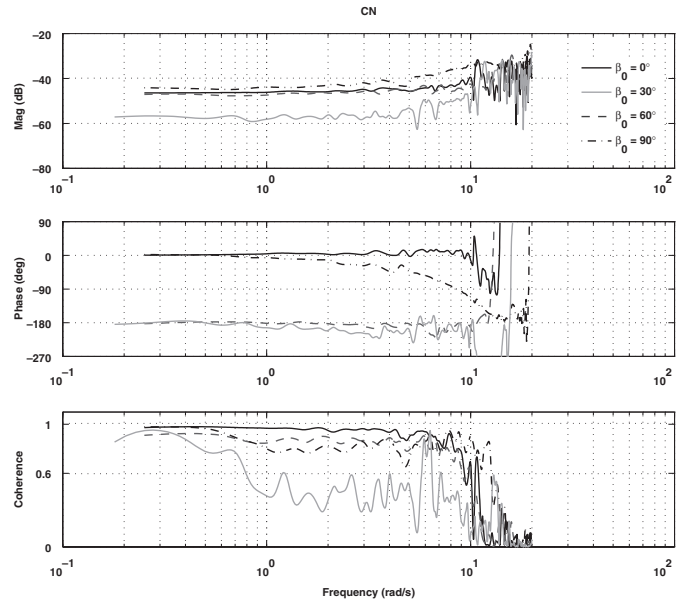


Figure 14. Frequency responses for sideslip offsets 0°, 30°, 60°, 90°.

frequency dependence of *CN* up through 9rad/sec satisfactorily. Several attempts to improve the high frequency coherence were made but were unsuccessful. The frequency sweep was revised to spend more time at high frequencies and a number of discrete frequency runs were made for frequencies, distributed over the range (9, 20) rad/sec. The discrete frequencies showed coherence near zero in the vicinity of the vortex shedding frequency, suggesting that there is little response to the forcing input compared to the independent vortex shedding effects at this frequency. Nevertheless, the computed response showed the expected 180° phase shift as the forcing frequency goes through the vortex shedding frequency.

### 5.3 Sideslip offsets

Variations in the transfer-function model with sideslip angle are of interest. Frequency responses for the yaw moment coefficient for reference sideslip angles every 30° in (0, 90°) are shown in Fig. 14. Differences in magnitude at low frequencies reflect differences in the magnitude of the slope of *CN*( $\beta$ ) at the reference angles, and the 180° differences in phase at low frequencies reflect the sign of the slope of *CN*( $\beta$ ) in Fig. 4. The responses at 0, 30°, and 60° are similarly flat with frequency but at 90° sideslip (short side facing the flow) the phase drops below -90° at high frequencies. This differs strongly from the phase behaviour around 0° and implies large phase lags not present around 0°. Transfer functions were fit to each of these cases. At 30° and 60°, the best fits were obtained with time-delay functions of the form,  $(a_1 s + a_0)e^{-\tau s}$ , while at 90° a second-order rational polynomial was required. Details of these fits can be found in Ref. 18. Although there are changes in the behaviour of the coefficients with sideslip angle, there are nevertheless some invariants. First, the time lag is approximately the same (0.113 sec) at all reference sideslip angles. In addition, the vortex shedding frequency was found to be invariant with sideslip angle.

## 6.0 SIMULATION

### 6.1 Yaw motion simulation

In some flight tests with the CONEX<sup>(7)</sup> the sling was attached at the hook with a swivel. With the swivel attachment, the CONEX spun



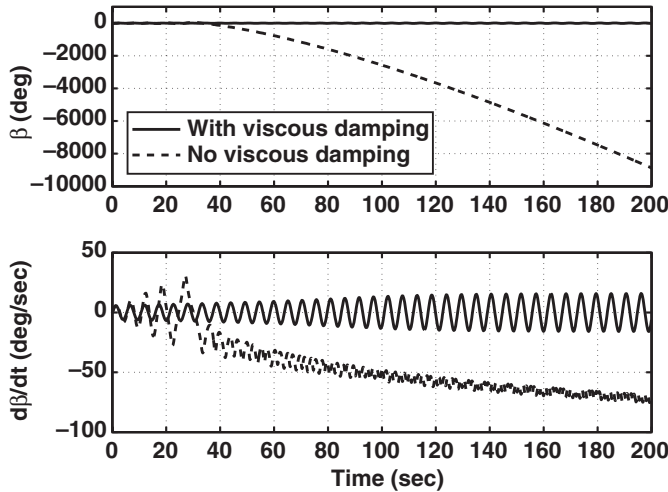


Figure 15. Effect of viscous damping, 60kt.

up to a steady-state yaw rate that increased with airspeed over the speed range of the tests. In this speed range, the yaw motions are decoupled from the pendulum motions and the pendulum modes are nondivergent. Consequently, a simple first test of the current model is to determine if it reproduces the observed yaw motions in a one-degree-of-freedom simulation. Previous simulation studies using the load static aerodynamics<sup>(9)</sup> were able to reproduce the flight pendulum motions but failed to reproduce the divergent sideslip angle, which is driven by the unsteady aerodynamics. The decoupled yaw degree of freedom is represented by:

$$I_{zz} \dot{r} = q Vol CN - K_r r \quad \dots (9(a))$$

$$\dot{\beta} = -r \quad \dots (9(b))$$

where the first term on the right is the aerodynamic yaw moment and the second term is swivel friction. Here,  $K_r$  was estimated at 1.245ft-lbs-sec,  $I_{zz} = 1376\text{ft-lbs-sec}^2$  for the flight test CONEX, Vol is the CONEX volume, and  $q$  is dynamic pressure.

The transfer function model for  $CN(\beta, \dot{\beta}, \tau)$  is given in Table 1. This model can be modified to account for the nonlinearity of the static aerodynamics over large angle changes by replacing  $CN_\beta \beta$  with the wind tunnel data,  $CN^{WT}(\beta, \alpha)$ , shown in Fig. 4. In addition, the parameter values for the model given in the table correspond to 60kt. At other airspeeds, the time dependence varies such that derivatives with respect to dimensionless time ( $t V/L$ ) are invariant. The final simulation model, valid at all airspeeds, is:

$$CN(s) = \frac{CN^{WT}(\alpha(s), \beta(s)) + \frac{V_{ref}}{V} a_1 s \Delta\beta}{\frac{V_{ref}}{V} \tau s + 1} \quad \dots (10(a))$$

or

$$\frac{V_{ref}}{V} \tau \dot{CN} + CN = CN^{WT}(\alpha, \beta) + \frac{V_{ref}}{V} a_1 \dot{\Delta\beta} \quad \dots (10(b))$$

where  $V_{ref}$  is the reference airspeed at which the coefficients were identified. Since this model applies in the vicinity of  $\beta = 0$ , it can be used for studies in which the CONEX is stabilised to trim at  $\beta = 0$ . However, the model will be applied at all  $\beta$  in the simulation tests

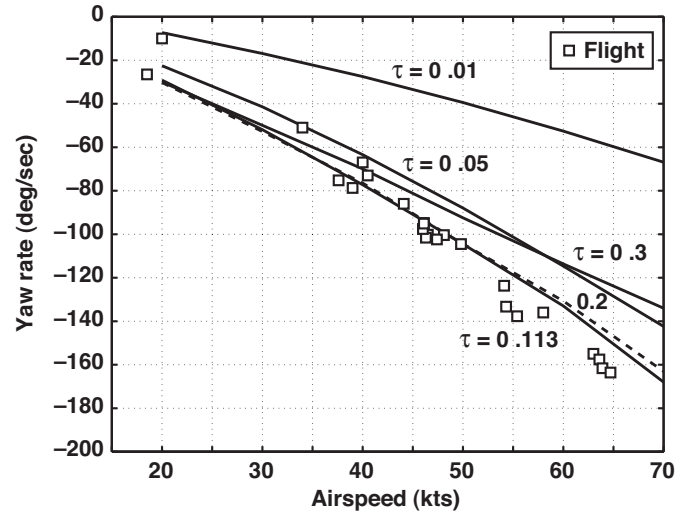


Figure 16. Comparison of steady-state yaw rate: simulation vs flight.

described next. This approximation neglects changes in the higher-order dynamics with sideslip but captures the essential lag of the denominator dynamics at all sideslip angles as well as the global variation in the static aerodynamics.

### 6.2 Results

Yaw-rate response to offset initial conditions at 60kt is shown in Fig. 15. The baseline model for CN results in a neutrally damped nondivergent sideslip oscillation around zero. However, if the viscous damping ( $a_1$ ) is removed, then the yaw rate is driven to a nonzero average steady-state value, which represents a balance between swivel friction and destabilising aerodynamic yaw moment due to the unsteady aerodynamics. After nulling the viscous damping, the swivel friction term was also adjusted to match the steady-state yaw rate measured in the flight data. Thus, there is some interchangeability between viscous damping and swivel friction in this validation exercise. Attempts to measure the swivel friction directly were inconclusive. The final simulation model is then simply the nonlinear static aerodynamics passed through a first-order lag.

Results were generated at other airspeeds over the range of the available flight data and yielded a similar response. A comparison of the simulation results for the steady-state average yaw rate with the available flight data over the speed range from 20 to 65kt is shown in Fig. 16. These show good agreement with flight over the range of the data. Simulation results at other values of the time constant,  $\tau$ , were generated to show sensitivity to  $\tau$ . These indicate a good match is obtained for  $\tau$  in the range 0.1 to 0.2 sec.

Figure 17 compares the body axes Y-force and Z-moment components with values derived from recent flight data recorded at 60kt. The CONEX is rotating in flight at a nearly steady rate of 157deg/sec. The plot shows data from one revolution of the CONEX for (1) flight, (2) the static aerodynamic wind tunnel data evaluated at the flight values of  $\alpha(t)$ ,  $\beta(t)$  and (3) the unsteady aerodynamic simulation model with the time constant approximately optimised to fit the flight data. First, Y-force is periodic at one period per revolution of the CONEX. The flight results cover the same range of magnitude as the static aerodynamics, and it is apparent from the zero crossings that the flight results lag the static aerodynamics. The optimised lag for the unsteady simulation model is 0.2 sec, and is seen to produce a good estimate of the flight results. The static

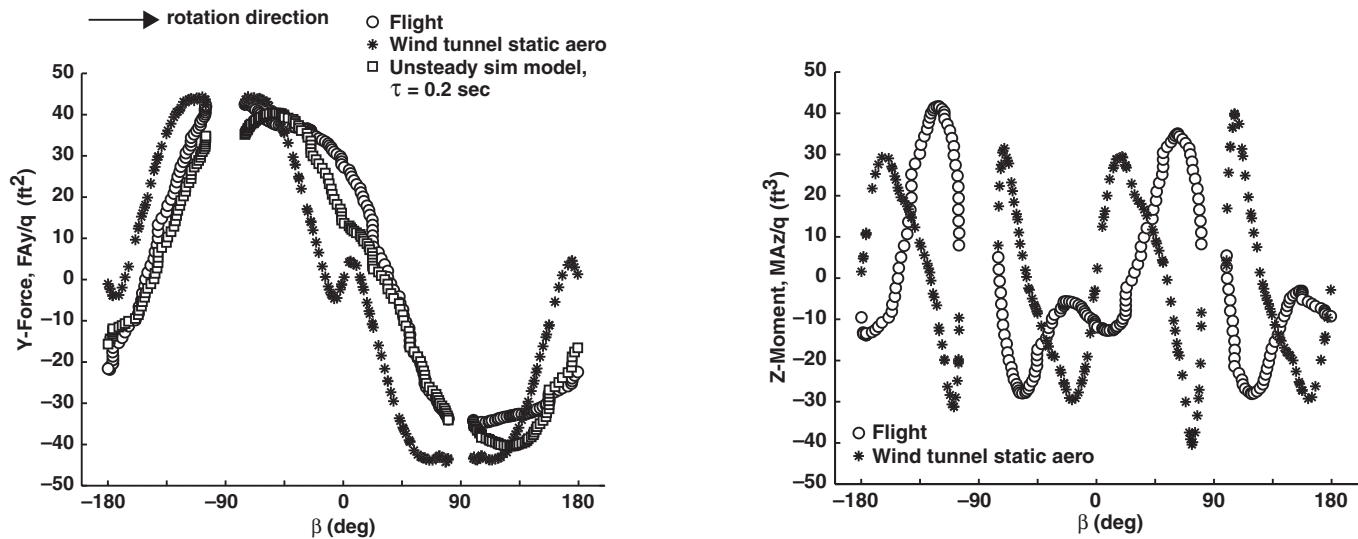


Figure 17. Comparison of aerodynamic components: simulation vs flight.

aerodynamics show a small double reversal at  $\beta = 0$ , which is attenuated in the unsteady simulation model, and this suppression of the double reversal matches the flight data. Note that the first-order transfer function attenuates frequencies above  $1/\tau$ , and that the double reversal is a high frequency event.

The Z-moment in Fig. 17 is also periodic but at four periods per revolution, which is close to the vortex shedding frequency. A comparison of the zero crossings indicates a lag in the flight data as expected, and the magnitude range of the flight data agrees well with the static aerodynamics. However, every second maximum in the flight data is greatly attenuated. In the static aerodynamics, this is associated with the maximum following passage through  $\pm 90$  deg (small side into the wind). This behaviour cannot be reproduced by the present simulation model, which would attenuate all extremes at this frequency. Possible causes of this mismatch are high-frequency behaviour not captured by the 2D aerodynamics, variations in the model with sideslip angle not captured by the present first-order model, behaviour of the rotational aerodynamics not revealed by the forced-oscillation aerodynamics, and measurement error.

These results for the unsteady aerodynamic model indicate limited success in reproducing the yaw moment. However, the model accounts quite well for the flight yaw behaviour over the speed range of the data, and for the aerodynamic lags.

## 7.0 SUMMARY AND CONCLUSIONS

This paper has presented preliminary results from the combined use of CFD and system identification techniques to obtain a transfer function model of the unsteady aerodynamics of the 6- × 6- × 8-ft CONEX cargo container for use in slung-load flight simulations. It is known that the aerodynamic instability of cargo containers is due to unsteady aerodynamic effects that result in frequency-dependent aerodynamics. However, current simulations lack a model of these effects and are unable to predict the critical speeds at which such loads become unstable.

This initial investigation was based on the 2D aerodynamics of the CONEX cross section owing to the large computation time required for 3D CFD computations, and the modelling was limited to the directional aerodynamics. Comparisons with the available 3D aerodynamic data indicated a close correspondence between 2D and 3D coefficients at low frequencies for side force and yaw moment. However, the background unsteady flow characteristics associated with vortex shedding differ strongly, these effects being greatly

attenuated in the 3D flow. It is not yet known what effect this has on variations of the coefficients with frequency.

The identification method results in a transfer function fit to frequency responses obtained from frequency sweep forced-oscillation aerodynamic data using an appropriate amplitude. This method is independent of the responsible flow phenomenon and is expected to apply to modelling the unsteady aerodynamics of bluff bodies generally. The transfer function is a linear model describing the behaviour of the aerodynamics around a mean attitude and is suited to problems in which there is a trim attitude, such as a stabilised load. Results for the CONEX indicated that a first-order function sufficed near zero sideslip angle (large face into the wind), and that there was some variation of the model with mean sideslip angle. However, the time lag was nearly invariant with sideslip. A final global model was formulated as a first-order transfer function with the identified time constant, and this was applied to the nonlinear global static aerodynamics available from wind tunnel data.

In flight, the CONEX suspended from a single point spins up to a nearly fixed steady-state yaw rate that varies with airspeed. A test of the model in a simulation of the yaw degree of freedom showed excellent agreement with the steady-state yaw rate from flight data over the airspeed range of the available data (65kt). A comparison with limited aerodynamic coefficient data derived from recent flight records showed that the global model matched the forces well after adjusting the time constant; that is, the forces are well represented as the lagged static aerodynamics. The flight yaw moment was matched as to lags, but there were significant differences in magnitude. It was noted that the flight yaw moment oscillated at four times the rotational frequency of the CONEX, and that high-frequency effects not captured by the theoretical model may account for this difference.

Despite the potential lack of realism associated with using the 2D aerodynamics in this application, the results of this study show the potential of the method to produce realistic simulation models of the aerodynamics of bluff-body slung loads capable of predicting their instabilities.

Important issues for further investigation include:

- (1) the extension to a model based on the 3D aerodynamics,
- (2) a method of accounting for variations in the dynamic model with sideslip angle, and
- (3) a demonstration that the model can reproduce 3D flight motions of the underslung CONEX at speeds above 65kt and predict the critical speed at which it develops pendulum instability or excessive amplitude due to the aerodynamics.

Recent flight-data records obtained from an instrumented CONEX at speeds up to 90kt are currently being analysed. This will provide a

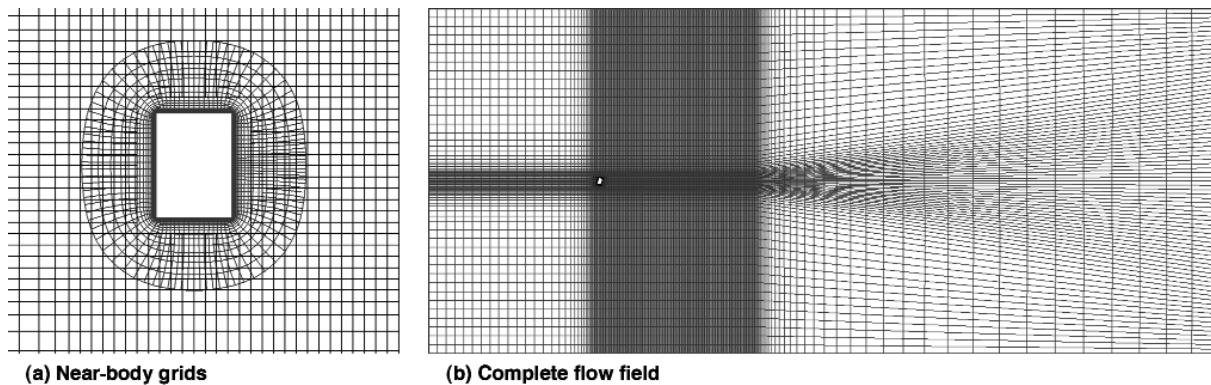


Figure A1. Grids for CFD simulation of 2D CONEX aerodynamics.

database documenting the behaviour of the CONEX as it approaches instability and provide for a more comprehensive validation of the current and future simulation models. In addition, a wind tunnel forced-oscillation rig capable of generating frequency sweeps has been designed and implemented at the Technion Institute of Technology, and may prove a satisfactory alternative source of the data needed for the 3D modelling.

## APPENDIX: CFD COMPUTATIONAL SCHEME

In the present work, the OVERFLOW-D code (version 1.5) was applied to study the flow field of the CONEX. It solves the compressible form of the Reynolds-averaged Navier-Stokes (RANS) equations using an implicit finite-difference approach with overset grids. This version of the code can simulate both 2D and 3D flows with arbitrary body motions. Solution convergence properties and accuracy are reduced for Mach numbers below 0.2, as is the case for most compressible RANS codes.

The code solves the equations in terms of dimensionless quantities. Density is normalised by free-stream density,  $\rho_\infty$ , position is normalised by a characteristic length,  $L$ , and velocities are normalised by the free-stream speed of sound,  $a_\infty$ . These result in dimensionless time,  $\bar{t} = ta_\infty/L$ , reduced frequencies and angular rates,  $\bar{\omega} = \omega L/V_\infty$ , and dimensionless pressures,  $\bar{P} = P/\rho_\infty a_\infty^2$ .

**Integration scheme.** The OVERFLOW-D code has various numerical integration schemes suitable for unsteady flow. The method chosen for this study is a scalar pentadiagonal scheme that is first-order accurate in time with fourth-order central differences in space. The code uses second- and fourth-order central difference dissipation terms to help maintain numerical stability. Details of the implicit solution method used by OVERFLOW-D can be found in Ref. 24.

**Grids.** The grid system for the CONEX 2D computations is shown in Fig. A1 for the near-body region and for the complete flow field of the simulation. Two structured overset grids are used, a body-conforming grid in the near-body region, and the background grid. The body-conforming grid is O-topology with 96 grid points in the circumferential direction and 41 points distributed normal to the body and extending one body length out from the body. This grid was generated using the hyperbolic grid-generation software HYPGEN<sup>(14)</sup>. The grid spacing normal to the body is 0.00005 body lengths at the body surface, and stretches to 0.05 body lengths at the edge of the near-body region using a tangent function. This grid moves with the body during body motions. During the solution, information at the boundary of the conforming grid is obtained by interpolating from the background grid.

The background grid consists of 301 points in the streamwise direction and 79 points across the flow. Points are uniformly

spaced out to two characteristic lengths in front, above, and below the CONEX cross section and 40 body lengths downstream. The grid spacing in this region approximately matches the spacing of the conformal grid at its outer boundary. Outside this region, the grid-point spacing is stretched out to the farfield boundaries in all directions. This grid-point distribution allows the vorticity to convect downstream with minimal diffusion. Grid spacing was further increased downstream of the body to minimise boundary reflections upstream. The complete flow field of the simulation extends 40 body lengths forward, above, and below the CONEX cross section, and 140 body lengths downstream.

**Turbulence.** Flow in the near-body conformal grid is assumed fully turbulent. OVERFLOW-D has several options for modelling boundary layer turbulence, and the Baldwin-Barth one-equation model<sup>(25)</sup> was selected for the present work. The flow throughout the background grid was assumed inviscid (no turbulence). This approximation is physically reasonable and helps minimise vorticity diffusion.

**Thin layer approximation.** The thin layer approximation of the RANS equations was adopted for flow in the near-body conformal grid. This approximation neglects circumferential derivative terms in the fluid shear stress, which cannot be well resolved with the current grid spacing. This approximation is appropriate for high Reynolds number flows, such as the present application<sup>(24)</sup>.

**Boundary conditions.** It was found that the appropriate choice of the far-field boundary condition and the distance to the far-field grid boundary were key in obtaining reliable solutions. Boundary conditions such as free-stream upstream, extrapolated downstream, and ‘supersonic/subsonic inflow/outflow’ (type 32) were evaluated. The type 32 boundary condition was found to have minimum effect on the unsteady solution. It uses the method of characteristics based on Riemann invariants to determine the flow variables at the boundaries. In addition, special grid treatment downstream of the box was needed. The uniform Cartesian mesh in the wake region tended to convect the bluff body shed vortex for a large distance downstream. The wake interacted with the downstream boundary, resulting in reflections upstream even with the use of the type 32 boundary condition. To minimise these reflections, the shed vortex was diffused by coarsening the mesh downstream.

**Time step.** The dimensionless time step was 0.025 for most of the present work. This value corresponds to 0.000291 sec real time at 60kt. Results were found insensitive to step sizes below 0.05.

**Validations.** Agreement of the 3D CONEX static aerodynamics with wind tunnel data is discussed in the text and in Ref. 18. For the square cylinder at  $\beta = 0$ , ( $Re = 3.9 \times 10^6$ ,  $M = 0.2$ ), the code with the same options used for the CONEX data predicted  $S_T = 0.13$  (experiments 0.13), mean  $CD = 2.1$  (experiments 1.9 to 2.1), rms  $CD$  fluctuations = 0.12 (experiments 0.1 to 0.2), and rms  $CS$  fluctuations = 1.5 (experiments 0.6 to 1.4). The experimental data

are quoted from Ref. 23. For the nearly square CONEX cross section (aspect ratio 1.4) at  $\beta = 0$ , ( $Re = 3.9 \times 10^6$ ,  $M = 0.2$ ), the code predicted  $S_T = 0.11$ , mean  $CD = 1.90$ , rms  $CD$  fluctuations = 0.10, rms  $CS$  fluctuations = 1.1, and rms  $CN$  fluctuations = 0.14. There are no experimental data for the CONEX cross section, but the unsteady coefficient characteristics are within the range of the experimental data for the square cross section and the Strouhal number is bracketed by experimental values for aspect ratios 1 and 2 in Ref. 19.

## REFERENCES

- Multiservice helicopter external air transport. **I** (Basic operations), **II** (Single point load rigging procedures), **III** (Dual point load rigging procedures), US Army FM-55-450-3,-4,-5. Feb. 1991.
- CHAN, D., FLOWER, J. and SIMPSON, A. Aerodynamically induced motions of bluff bodies suspended beneath helicopters, Final report, Report AD, Department of Aeronautical Engineering, University of Bristol, Bristol, UK October 1975.
- SIMPSON, A. and FLOWER, J. Unsteady aerodynamics of oscillating containers and application to the problem of dynamic stability of helicopter underslung loads, AGARD CP235, November 1978.
- WATKINS, T., SINACORI, J. and KESLER, D. Stabilisation of externally slung helicopter loads, US Army Air Mobility Research and Development Laboratory TR-74-42, Aug. 1974.
- SAMPATH, P. Dynamics of a Helicopter-Slung Load System. Ph.D. thesis. Department of Aerospace Engineering, U Maryland, College Park, Md, January 1980.
- RONEN, T. Dynamics of a Helicopter With a Sling Load. Ph.D. thesis, Stanford University, Stanford, California, August 1985. Also RONEN, T., BRYSON, A. and HINDSON, W. Dynamics of a helicopter with a sling load, AIAA 86-2288, August 1986.
- CICOLANI, L.S., MCCOY, A.H., SAHAI, R., TYSON, P., TISCHLER, M.B., RONEN, A. and TUCKER, G. Flight test identification and simulation of a UH-60A helicopter and slung load, *J American Helicopter Society*, 2001, **46**, pp 140-160.
- RONEN, A., CECUTTA, S. and YAFFE, R. Wind tunnel tests of cube and CONEX models, Report TAE-844, Faculty of Aerospace Engineering, Technion Institute of Technology, Haifa, Israel, November 1999.
- TYSON, P., CICOLANI, L.S., TISCHLER, M.B., ROSEN, A., LEVINE, D. and DEARING, M. Simulation prediction and flight validation of UH-60A Black Hawk slung load characteristics, 55th AHS Forum Proceedings, May 1999.
- BUNING, P.G., CHIU, I.T., OBAYASHI, S., RIZK, Y.M. and STEGER, J.L. Numerical simulation of the integrated space shuttle vehicle in ascent, AIAA 88-4359, August 1988.
- PALMER, J., BUNING, P.G., YANOWITZ, H. and VENKATAPATHY, E. Three-dimensional computational analysis of complex launch vehicle configurations, *J Spacecraft and Rockets*, 1996, **33** pp 49-53.
- MEAKIN, R. Moving grid overset grid methods for complete aircraft tiltrotor simulations, AIAA 93-3350, July 1993.
- AHMAD, J. and DUQUE, E.P.N. Helicopter rotor blade computation in unsteady flows using moving overset grids, *J Aircr*, 1996, **33**, pp 54-60.
- CHAN, W.M. The OVERGRID interface for computational simulations on OVERSET grids, AIAA 2002-3188, June 2002.
- THOMAS, T.G. and WILLIAMS J.J.R. Large eddy simulation of vortex shedding from a cubic obstacle, *J Aerospace Engineering*, 1999, **12**, pp 113-120.
- Methodology – STAR-CD Version 3.15, Computational Dynamics Limited, 2001. URL: [www.adapco.com](http://www.adapco.com).
- DUQUE, E.P.N., GORDON, R., BERRY, M.D., CICOLANI, L.S. and ROSEN, A. Reynolds-averaged Navier-Stokes simulations of helicopter slung loads. Proceedings, AHS 4th Decennial Specialist's Conference on Aeromechanics. January 2004.
- CICOLANI, L.S., DA SILVA, J.G.A., DUQUE, E.P.N. and TISCHLER, M.B. Unsteady aerodynamic model of a cargo container for slung load simulation: Preliminary aerodynamic data and model identification, NASA TM-2004-212817, May 2004.
- OKAJIMA A. Strouhal numbers of rectangular cylinders, *J Fluid Mech*, 1982, **123**, pp 379-398.
- Northern Arizona University, Department of Mechanical Engineering, Flagstaff Arizona, (accessed April 2004). URL [http://www.cet.nau.edu/~end2/Research/Rotorcraft/cube/mou\\_spr03/static\\_pressure\\_x.mpg](http://www.cet.nau.edu/~end2/Research/Rotorcraft/cube/mou_spr03/static_pressure_x.mpg)
- [www.cet.nau.edu/~end2/Research/Rotorcraft/cube/mou\\_spr03/static\\_pressure\\_z.mpg](http://www.cet.nau.edu/~end2/Research/Rotorcraft/cube/mou_spr03/static_pressure_z.mpg)
- [www.cet.nau.edu/~end2/Research/Rotorcraft/cube/mou\\_spr03/motion\\_pressure\\_x.mpg](http://www.cet.nau.edu/~end2/Research/Rotorcraft/cube/mou_spr03/motion_pressure_x.mpg)
- [www.cet.nau.edu/~end2/Research/Rotorcraft/cube/mou\\_spr03/motion\\_pressure\\_z.mpg](http://www.cet.nau.edu/~end2/Research/Rotorcraft/cube/mou_spr03/motion_pressure_z.mpg)
- TISCHLER, M.B. and CAUFFMAN, M.G. Frequency-response method for rotorcraft system identification: Flight applications to BO-105 coupled rotor/fuselage dynamics, *J of the American Helicopter Society*, 1992, **37**, pp 3-17.
- TISCHLER, M.B. and CAUFFMAN, M.G. Comprehensive identification from frequency responses: An interactive facility for system identification and verification, NASA Conference Publication 10149, Moffett Field, California, September 1994.
- ERCOFTAC Test Case LES2: Flow past a long square cylinder. U. of Surrey, Guildford, UK February 1998. URL <http://vortex.mech.surrey.ac.uk/LESig/les2/> (accessed April 2004).
- PULLIAM, T.H. and STEGER, J.L. Implicit finite-difference simulations of three dimensional compressible flow, *AIAA J.*, 1980, **18**, pp 159-167.
- BALDWIN, B.S. and BARTH, T.J. A One-equation turbulence transport model for high Reynolds number wall-bounded flows, NASA TM-102847, August 1990.